Smaller fish species in a warm and oxygen-poor Humboldt Current system

Renato Salvatteci, Ralph R Schneider, Eric Galbraith, David Field, Thomas Blanz, Thorsten Bauersachs, Xavier Crosta, Philippe Martinez, Vincent Echevin, Florian Scholz, et al.

Science
January 2022, Volume 375 Issue 6576 Pages 101-104
https://doi.org/10.1126/science.abj0270
https://archimer.ifremer.fr/doc/00747/85887/

Smaller fish species in a warm and oxygen-poor Humboldt Current system

Salvatteci Renato [1, *], Schneider Ralph R. [2], Galbraith Eric [3, 4], Field David [5], Blanz Thomas [2], Bauersachs Thorsten [2], Crosta Xavier [6], Martinez Philippe [6], Echevin Vincent [7], Scholz Florian [8], Bertrand Arnaud [9]

[1] Center for Ocean and Society, Christian-Albrechts-University, Kiel, Germany.
[2] Institute of Geosciences, Christian-Albrechts-University, Kiel, Germany.
[3] Earth and Planetary Sciences, McGill University, Montreal, QC, Canada.
[4] Institut de Ciència i Tecnologia Ambientals (ICTA-UAB), Universitat Autònoma de Barcelona, 08193 Cerdanyola del Vallès, Barcelona, Spain.
[5] College of Natural Sciences, Hawaii Pacific University, Kaneohe, HI, USA.
[6] Université de Bordeaux, CNRS, EPHE, UMR 5805 EPOC, Pessac, France.
[7] Sorbonne Université, LOCEAN-IPSL, CNRS/IRD/MNHN, 4 place Jussieu, 75252 Paris, France.
[8] GEOMAR Helmholtz Centre for Ocean Research Kiel, Germany.
[9] Institut de Recherche pour le Développement (IRD), MARBEC, University Montpellier, CNRS, Ifremer, IRD, Sète, France.

* Corresponding author : Renato Salvatteci, email address : rsalvatteci@kms.uni-kiel.de

Abstract :

Climate change is expected to result in smaller fish size, but the influence of fishing has made it difficult to substantiate the theorized link between size and ocean warming and deoxygenation. We reconstructed the fish community and oceanographic conditions of the most recent global warm period (last interglacial; 130 to 116 thousand years before present) by using sediments from the northern Humboldt Current system off the coast of Peru, a hotspot of small pelagic fish productivity. In contrast to the present-day anchovy-dominated state, the last interglacial was characterized by considerably smaller (mesopelagic and goby-like) fishes and very low anchovy abundance. These small fish species are more difficult to harvest and are less palatable than anchovies, indicating that our rapidly warming world poses a threat to the global fish supply.

Reduced body size has been postulated as a universal ecological response to warming in aquatic systems (*1*, *2*). Shrinking body size among marine ectotherms has been hypothetically linked to temperature as predicted by Bergmanns's rule, with smaller body sizes associated with warmer temperatures (*3*) and reduced oxygen availability (*4*). The energetic demand of fish – and thus their oxygen consumption – increases with water temperature, yet oxygen solubility is reduced in warmer waters (*5*). Smaller fish maintain high activity in warm, oxygen-poor waters (*6*), and are therefore expected to increase in relative abundance with future climate change (*7*). However, the degree to which an increase in temperature and decrease in oxygen will increase the proportion of small sized species (i.e. species shift hypothesis) relative to a decrease in mean body size at the population scale (i.e. population body size hypothesis) remains unclear (*2*).

We tested the relationships between water temperature, subsurface oxygen, fish species abundance and size using paleoceanographic records from the Humboldt Current System. In this upwelling system, an extremely high biomass of anchovy (*Engraulis ringens*) has yielded up to 15% of the global annual fish catch (*8*). Model projections suggest that by the end of the 21st century, the Humboldt Current will be warmer and less oxygenated (*9*) compared to modern times. Concerningly, pre-fishery data have revealed biological tipping points that led to repeated multifarious regime shifts in the Humboldt Current over past centuries (*10*, *11*), but are not reproduced by ecological modelling experiments (*12*). Studies of sediment cores have the potential to reveal the state and dynamics of past climates and ecosystems on multiple timescales (*13*). In particular, fishery-independent data from sediment records offer the opportunity to better understand the response of the fish community to a warmer world.

We focus on the last interglacial or MIS5e, a globally warmer-than-present period, and combine multiple sedimentary paleo-proxies including alkenone unsaturation index ($U^{k'}_{37}$) and tetraether index of tetraethers consisting of 86 carbon atoms (TEX^{H}_{86}) derived temperatures, $\delta^{15}N$, total organic carbon, biogenic silica measurements and diatom assemblages as well as fish vertebrae and bones, to characterize the Humboldt Current at that time in comparison to the Holocene (Figs. S1-S4).

Our paleo-reconstruction shows that environmental changes during the last interglacial (Fig. 1 e-h) were similar to the RCP8.5 projections to 2100 (Fig. 1 a-d; Fig. S5), including a similar magnitude of warming, intensified subsurface oxygen depletion, strengthened vertical density gradients, and comparable primary production. During the last interglacial, water temperatures adjacent to central Peru were on average ~2 ºC warmer than during the Holocene (Fig. 1a, e; Fig. S1), plausibly caused by a persistent El Niño-like state (*14*). Elevated $\delta^{15}N$ is consistent with intensified water column denitrification during the last interglacial, as would be expected with a more intense oxygen minimum zone (Fig. 1f, Fig. S2), which is also supported by higher concentrations of redox sensitive metals (*14*). Also, more intense stratification and deeper thermocline occurred compared to the Holocene (Fig. 1g), as indicated by the difference between the alkenone (temperatures at and above the thermocline) and the TEX^{H}_{86} (temperatures below the thermocline). Finally, productivity indicators are remarkably similar between the two interglacials (Fig. 1h, Fig. S2), suggesting similar rates of nutrient supply through upwelling activity.

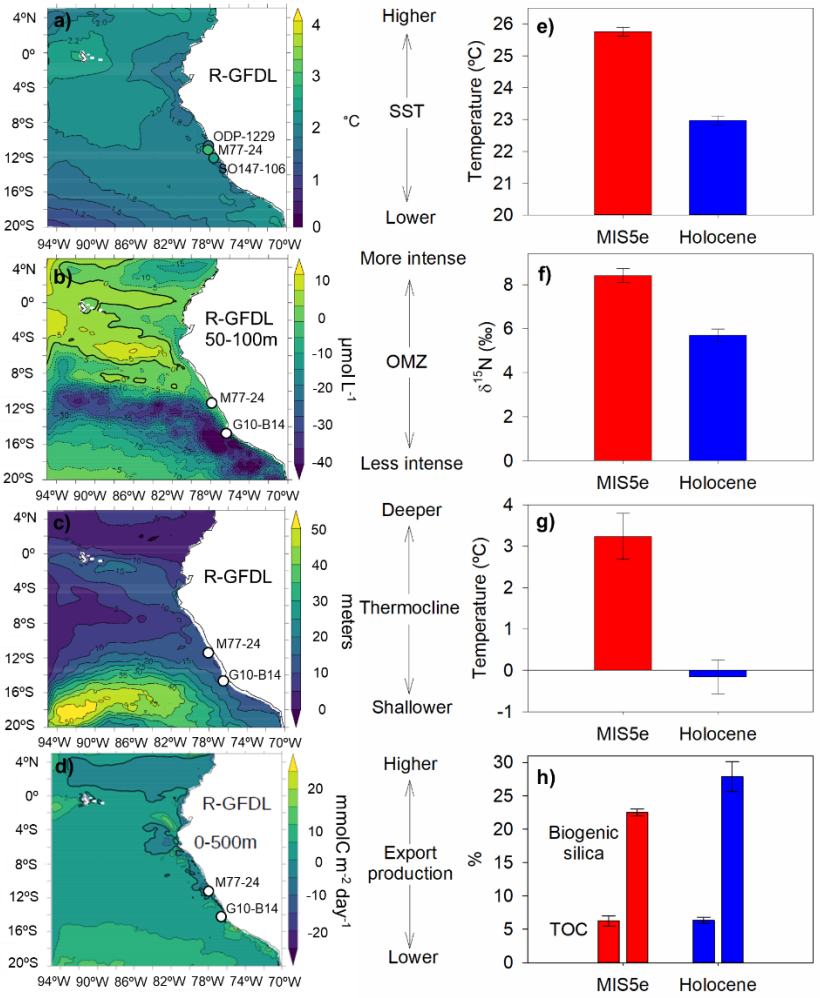

Figure 1. Comparison of model projections for the RCP 8.5 scenario, based on the Geophysical Fluid Dynamic Laboratory (GFDL) - Earth system model (2086-2100 average minus 2006-2020), with paleoceanographic data for the Holocene and the last interglacial (M77/2-24). a, R-GFDL SST, the colored circles indicate the SST difference between the last interglacial and Holocene alkenone-derived SST in cores ODP-1229 (*14*), SO147-106 (*15*) and M77/2-24. **b,** Oxygen concentration (µmol L^{-1}) between 50-100 meters depth. **c,** depth of the 20ºC isotherm as a proxy for thermocline depth. **d,** R-GFDL Primary productivity (mmolC m^{-2} day^{-1}) in the upper 500 meters of the water column. The white circles in b, c and d indicate the position of M77/2-24 and G10-B14. **e,** Alkenone-derived SST average during the last interglacial and Holocene (M77/2-24). **f,** $\delta^{15}N$ average during the last interglacial and Holocene as a proxy for water column denitrification (M77/2-24). **g,**

Difference between alkenone and TEX_{86} derived temperatures, where higher values indicate a deeper thermocline (M77/2-24). **h,** Average values (±2 standard error) of total organic carbon (TOC) and biogenic silica during the last interglacial and Holocene (M77/2-24), average biogenic silica for the Holocene from (*16*).

The fish community inhabiting the Humboldt Current during the last interglacial differed dramatically from the communities found during the Holocene (Fig. 2; Fig. S3, S4) and the observational period. Whereas anchovy have clearly dominated the fish community throughout the Holocene, they only occurred in minor proportions during the last interglacial. By contrast, goby-like species accounted for almost 60 % of the fish vertebrae assemblage during the last interglacial (Fig. 2). Gobies are small fishes specially adapted to survive in hypoxic or even sulfidic environments, conditions that are avoided by most organisms (*17*). Our inference of goby-like fishes dominating the Humboldt Current during the last interglacial is consistent with genetic analysis suggesting that a population expansion of the goby *Elacatinus puncticulatus* began at 170-130 Kyr in the Tropical Eastern Pacific (*18*).

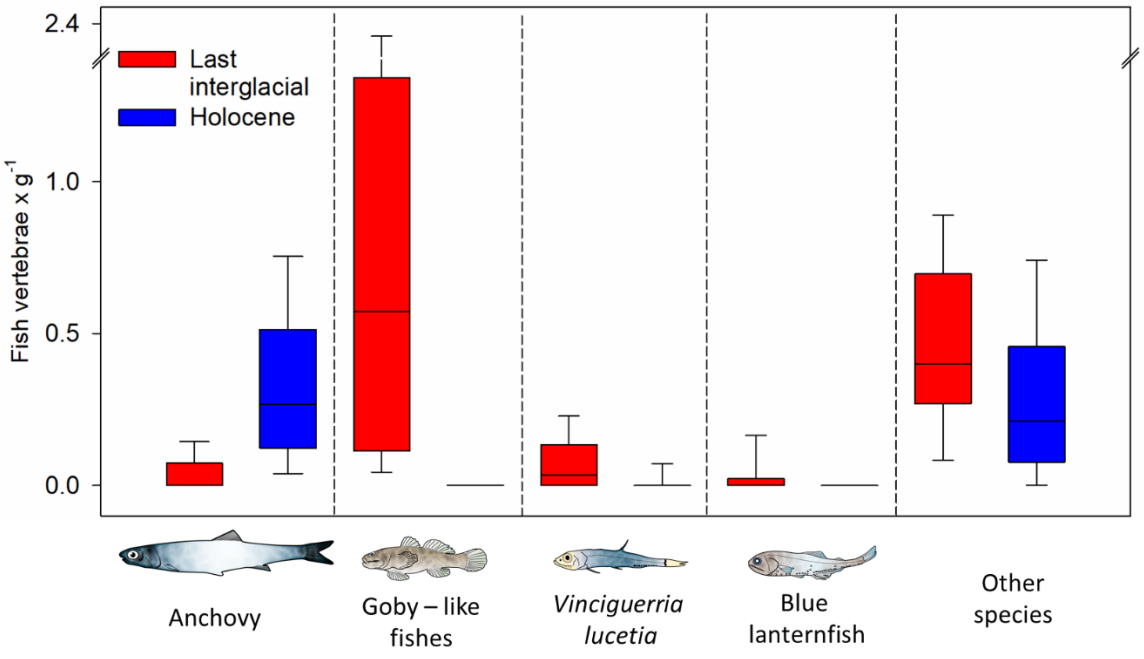

Figure 2. No-analog fish community in a warmer world. Fish vertebrae abundances during the last interglacial and the Holocene. Goby-like and mesopelagic fishes (i.e. *Vinciguerria lucetia* and blue lanternfish (*Tarletonbeania crenularis*)) were abundant during the last interglacial. The "other species" category includes vertebrae from unidentified juvenile fish, from mesopelagic and unidentified fishes.

Similar to the goby-like fishes, mesopelagic fishes were highly abundant at our coastal site during the last interglacial (Fig. 2). The vertebrae assemblage during the last interglacial included vertebrae from *Vinciguerria lucetia*, blue lanternfish and many other small vertebrae, likely belonging to other mesopelagic species (Fig. 2). This high coastal abundance is in marked contrast with modern observations showing that mesopelagic fishes are located offshore associated with upwelling fronts (*19*). Mesopelagic fishes have evolved physiological and morphological adaptations to live in oxygen-deficient waters, perform diel vertical migration into the oxygen minimum zone, and can tolerate episodes of severe hypoxia (*19*), leading us to speculate that their incursion to coastal waters was linked to the intensification of mid-depth oxygen depletion. Although degradation of fish debris does occur in the sedimentary column (*20*), small and thin vertebrae are more susceptible to degradation, which would actually lead to an underestimation of small fish during the last interglacial, opposite to what is observed. Furthermore, the index of preservation of vertebrae was higher during the last interglacial suggesting good vertebrae preservation (Fig. S6).

Our reconstruction reveals a major shift in species in response to warming, but does not support a decrease in population body size, given that we did not find any significant reduction in vertebrae widths of a given species during the last interglacial (Fig. 3a; Table S2). A generalized additive model shows a significant ($p<0.001$) non-linear effect of the

interaction of oxygen and temperature on the inferred average fish body size (Figure 3b). The smallest vertebrae (mostly goby-like fishes) are associated with the highest reconstructed water temperatures and lowest inferred oxygen concentration (i.e. last interglacial conditions). By contrast, the largest vertebrae (mostly anchovy) are associated with the lowest temperatures and lowest oxygen concentrations (i.e. some periods during the Holocene including the last century) when strong upwelling led to low temperatures, promoting increased productivity and related deoxygenation (*10*, *11*). Thus, smaller fish species, rather than smaller fishes from the same species, flourished in the Humboldt Current, suggesting the possibility of an environmentally triggered tipping point beyond which anchovy ceases to be a dominant part of the ecosystem.

The overall shift to smaller body size is consistent with aspects of the Gill Oxygen Limitation theory (GOLT), which occurred through a shift to smaller species rather than a shrinking of the same species. The GOLT argues that the geometrical constraints of gills reduce the rate at which ectotherms can extract oxygen from water, relative to their body size, as they become larger (*6*). During the last interglacial, the heightened oxygen demand caused by warmer water may have required anchovy, which reproduce in waters colder than 25ºC (*21*), to shift poleward to satisfy oxygen demand. In contrast, smaller goby-like fishes have larger gills surfaces in relation to their body volume and can therefore withstand low oxygen waters.

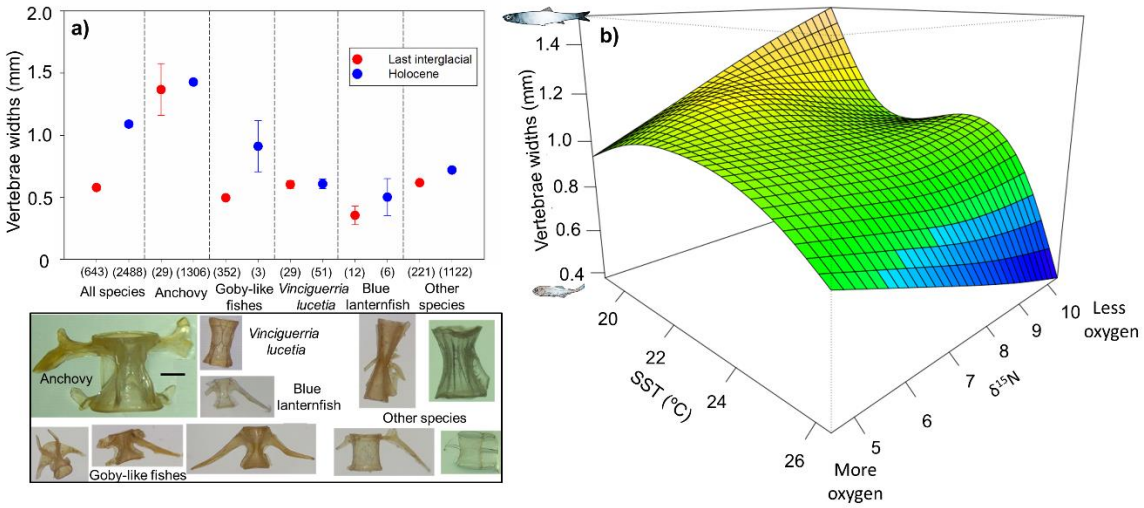

Figure 3. Small fish in a warm ocean. a, Average values (± 2 standard error) of fish vertebrae widths as an indicator of fish size for the Holocene and the last interglacial, values in parentheses indicate the number of vertebrae measured. In some cases, the error bars overlap with the symbol. Note that the goby-like fishes may include multiple species. Pictures of the most abundant fish vertebrae for the Holocene and the last interglacial found in M77/2-024 are also shown (bar represents 1 mm). **b,** Generalized additive model (GAM) describing the significant relationship between vertebrae width and an interaction between temperature and oxygen. A linear negative correlation between vertebrae size and temperatures reiterates the relationship (Fig. S7).

Our results are concerning, as recent studies indicate that the environmental conditions and fish communities in the Humboldt Current are progressing toward those we reconstructed during the last interglacial. In the last decades, midwater oxygen concentrations have decreased off Peru, the abundance of several warm-water mesopelagic species like *V. lucetia* has increased (*22*), and anchovy biomass and landings have steadily decreased despite a flexible and adaptive fishery management strategy (*23*). Conditions may therefore be approaching the tipping-point in fish community suggested by our analysis. Fishery managers, global markets and other stakeholders will need to develop adaptive strategies to cope with

this threat to the Humboldt Current food source, while raising vigilance regarding similar climate-driven shifts in fish communities elsewhere.

References and notes

1. W. W. L. Cheung, J. L. Sarmiento, J. Dunne, T. L. Frölicher, V. W. Y. Lam, M. L. Deng Palomares, R. Watson, D. Pauly, Shrinking of fishes exacerbates impacts of global ocean changes on marine ecosystems. *Nature Clim Change*. **3**, 254–258 (2013).

2. M. Daufresne, K. Lengfellner, U. Sommer, Global warming benefits the small in aquatic ecosystems. *PNAS*. **106**, 12788–12793 (2009).

3. G. Hunt, K. Roy, Climate change, body size evolution, and Cope's Rule in deep-sea ostracodes. *Proceedings of the National Academy of Sciences*. **103**, 1347–1352 (2006).

4. H. O. Portner, R. Knust, Climate Change Affects Marine Fishes Through the Oxygen Limitation of Thermal Tolerance. *Science*. **315**, 95–97 (2007).

5. C. Deutsch, J. L. Penn, B. Seibel, Metabolic trait diversity shapes marine biogeography. *Nature*. **585**, 557–562 (2020).

6. D. Pauly, The gill-oxygen limitation theory (GOLT) and its critics. *Sci. Adv.* **7**, eabc6050 (2021).

7. J. G. Rubalcaba, W. C. E. P. Verberk, A. J. Hendriks, B. Saris, H. A. Woods, Oxygen limitation may affect the temperature and size dependence of metabolism in aquatic ectotherms. *Proc Natl Acad Sci USA*. **117**, 31963–31968 (2020).

8. FAO, *The State of World Fisheries and Aquaculture 2020* (FAO, 2020; http://www.fao.org/documents/card/en/c/ca9229en).

9. V. Echevin, M. Gévaudan, D. Espinoza-Morriberón, J. Tam, O. Aumont, D. Gutierrez, F. Colas, Physical and biogeochemical impacts of RCP8.5 scenario in the Peru upwelling system. *Biogeosciences*. **17**, 3317–3341 (2020).

10. R. Salvatteci, D. Field, D. Gutiérrez, T. Baumgartner, V. Ferreira, L. Ortlieb, A. Sifeddine, D. Grados, A. Bertrand, Multifarious anchovy and sardine regimes in the Humboldt Current System during the last 150 years. *Global Change Biology*. **24**, 1055–1068 (2018).

11. R. Salvatteci, D. Gutierrez, D. Field, A. Sifeddine, L. Ortlieb, S. Caquineau, T. Baumgartner, V. Ferreira, A. Bertrand, Fish debris in sediments from the last 25 kyr in the Humboldt Current reveal the role of productivity and oxygen on small pelagic fishes. *Progress in Oceanography*. **176**, 102–114 (2019).

12. W. W. L. Cheung, J. Bruggeman, J. Butenschön, in *Impacts of climate change on fisheries and aquaculture: Synthesis of current knowledge, adaptation and mitigation options* (Food and Agriculture Organization of United Nation, 2018), pp. 63–85.

13. M. Yasuhara, H.-H. M. Huang, P. Hull, M. C. Rillo, F. L. Condamine, D. P. Tittensor, M. Kučera, M. J. Costello, S. Finnegan, A. O'Dea, Y. Hong, T. C. Bonebrake, N. R. McKenzie, H. Doi, C.-L. Wei, Y. Kubota, E. E. Saupe, Time Machine Biology. *Oceanography*. **33**, 16–28 (2020).

14. S. Contreras, C. B. Lange, S. Pantoja, G. Lavik, D. Rincón-Martínez, M. M. Kuypers, A rainy northern Atacama Desert during the last interglacial. *Geophysical Research Letters*. **37** (2010), doi:10.1029/2010GL045728.

15. B. Rein, F. Sirocko, A. Lückge, L. Reinhardt, A. Wolf, W.-C. Dullo, in *The Climate of Past Interglacials*, F. Sirocko, M. Claussen, M. Sánchez Goñi, T. Litt, Eds. (2007), pp. 305–321.

16. K. Doering, Z. Erdem, C. Ehlert, S. Fleury, M. Frank, R. Schneider, Changes in diatom productivity and upwelling intensity off Peru since the Last Glacial Maximum: Response to basin-scale atmospheric and oceanic forcing. *Paleoceanography*. **31** (2016), doi:10.1002/2016PA002936.

17. A. Salvanes, A. Utne-Palm, B. Currie, V. Braithwaite, Behavioural and physiological adaptations of the bearded goby, a key fish species of the extreme environment of the northern Benguela upwelling. *Mar. Ecol. Prog. Ser.* **425**, 193–202 (2011).

18. E. R. Sandoval-Huerta, R. G. Beltrán-López, C. R. Pedraza-Marrón, M. A. Paz-Velásquez, A. Angulo, D. R. Robertson, E. Espinoza, O. Domínguez-Domínguez, The evolutionary history of the goby Elacatinus puncticulatus in the tropical eastern pacific: Effects of habitat discontinuities and local environmental variability. *Molecular Phylogenetics and Evolution*. **130**, 269–285 (2019).

19. R. Cornejo, R. Koppelmann, Distribution patterns of mesopelagic fishes with special reference to Vinciguerria lucetia Garman 1899 (Phosichthyidae: Pisces) in the Humboldt Current Region off Peru. *Marine Biology*. **149**, 1519–1537 (2006).

20. R. Salvatteci, D. B. Field, T. Baumgartner, V. Ferreira, D. Gutierrez, Evaluating fish scale preservation in sediment records from the oxygen minimum zone off Peru. *Paleobiology*. **38**, 52–78 (2012).

21. R. Castillo, L. Dalla Rosa, W. García Diaz, L. Madureira, M. Gutierrez, L. Vásquez, R. Koppelmann, Anchovy distribution off Peru in relation to abiotic parameters: A 32-year time series from 1985 to 2017. *Fish Oceanogr*. **28**, 389–401 (2019).

22. J. Argüelles, R. Tafur, A. Taipe, P. Villegas, F. Keyl, N. Dominguez, M. Salazar, Size increment of jumbo flying squid Dosidicus gigas mature females in Peruvian waters, 1989–2004. *Progress in Oceanography*. **79**, 308–312 (2008).

23. R. Oliveros-Ramos, M. Ñiquen, J. Csirke, R. Guevara-Carrasco, in *Adaptive Management of Fisheries in Response to Climate Change* (FAO, Rome, 2020), *FAO Fisheries and Aquaculture Technical Paper 667*.

24. P. Penven, L. Debreu, P. Marchesiello, J. C. McWilliams, Evaluation and application of the ROMS 1-way embedding procedure to the central California upwelling system. *Ocean Modelling*. **12**, 157–187 (2006).

25. A. F. Shchepetkin, J. C. McWilliams, Correction and commentary for "Ocean forecasting in terrain-following coordinates: Formulation and skill assessment of the regional ocean modeling system" by Haidvogel et al., J. Comp. Phys. 227, pp. 3595–3624. *Journal of Computational Physics*, 16 (2009).

26. C. M. Risien, D. B. Chelton, A Global Climatology of Surface Wind and Wind Stress Fields from Eight Years of QuikSCAT Scatterometer Data. *Journal of Physical Oceanography*. **38**, 2379–2413 (2008).

27. F. Scholz, J. McManus, A. Mix, C. Hensen, R. Schneider, The impact of ocean deoxygenation on the ocean's iron supply. *Nature Geoscience*. **7**, 433–437 (2014).

28. L. E. Lisiecki, M. E. Raymo, A Pliocene-Pleistocene stack of 57 globally distributed benthic δ18O records. *Paleoceanography*. **20**, PA1003 (2005).

29. R. Salvatteci, D. Field, A. Sifeddine, L. Ortlieb, V. Ferreira, T. Baumgartner, S. Caquineau, F. Velazco, J. L. Reyss, J. A. Sanchez-Cabeza, D. Gutierrez, Cross-stratigraphies from a seismically active mud lens off Peru indicate horizontal extensions of laminae, missing sequences, and a need for multiple cores for high resolution records. *Marine Geology*. **357**, 72–89 (2014).

30. R. Salvatteci, R. R. Schneider, T. Blanz, E. Mollier-Vogel, Deglacial to Holocene Ocean Temperatures in the Humboldt Current System as Indicated by Alkenone Paleothermometry. *Geophysical Research Letters*. **46** (2019), doi:10.1029/2018gl080634.

31. G. Wefer, P. Heinze, E. Suess, in *Proceedings of the Ocean Drilling Program, Scientific Results, Vol. 112* (1990).

32. R. Salvatteci, D. Gutierrez, A. Sifeddine, L. Ortlieb, E. Druffel, M. Boussafir, R. Schneider, Centennial to millennial-scale changes in oxygenation and productivity in the Eastern Tropical South Pacific during the last 25 000 years. *Quaternary Science Reviews*. **131**, 102–117 (2016).

33. E. Mollier-Vogel, P. Martinez, T. Blanz, R. Robinson, S. Desprat, J. Etourneau, K. Charlier, R. Schneider, Mid-Holocene deepening of the Southeast Pacific oxycline. *Global and Planetary Change*. **172**, 365–373 (2018).

34. J. Etourneau, R. Schneider, T. Blanz, P. Martinez, Intensification of the Walker and Hadley atmospheric circulations during the Pliocene–Pleistocene climate transition. *Earth and Planetary Science Letters*. **297**, 103–110 (2010).

35. T. Blanz, K.-C. Emeis, H. Siegel, Controls on alkenone unsaturation ratios along the salinity gradient between the open ocean and the Baltic Sea. *Geochimica et Cosmochimica Acta*. **69**, 3589–3600 (2005).

36. P. J. Müller, G. Kirst, G. Ruhland, I. von Storch, A. Rosell-Melé, Calibration of the alkenone paleotemperature index U37K` based on core-tops from the eastern South Atlantic and the global ocean (60°N-60°S). *Geochimica et Cosmochimica Acta*. **62**, 1757–1772 (1998).

37. G. Leduc, R. Schneider, J.-H. Kim, G. Lohmann, Holocene and Eemian sea surface temperature trends as revealed by alkenone and Mg/Ca paleothermometry. *Quaternary Science Reviews*. **29**, 989–1004 (2010).

38. E. C. Hopmans, S. Schouten, R. D. Pancost, J. S. S. Damste, Analysis of intact tetraether lipids in archaeal cell material and sediments by high performance liquid chromatography/atmospheric pressure chemical ionization mass spectrometry. *Rapid Commun. Mass Spectrom.*, 5 (2000).

39. X.-L. Liu, R. E. Summons, K.-U. Hinrichs, Extending the known range of glycerol ether lipids in the environment: structural assignments based on tandem mass spectral fragmentation patterns: Extending the known range of glycerol ether lipids in the environment. *Rapid Commun. Mass Spectrom.* **26**, 2295–2302 (2012).

40. J.-H. Kim, New indices and calibrations derived from the distribution of crenarchaeal isoprenoid tetraether lipids: Implications for past sea surface temperature reconstructions. *Geochimica et Cosmochimica Acta*, 16 (2010).

41. S. Schouten, E. C. Hopmans, E. Schefuß, J. S. Sinninghe Damsté, Distributional variations in marine crenarchaeotal membrane lipids: a new tool for reconstructing ancient sea water temperatures? *Earth and Planetary Science Letters*. **204**, 265–274 (2002).

42. R. A. Lopes dos Santos, M. I. Spooner, T. T. Barrows, P. De Deckker, J. S. Sinninghe Damsté, S. Schouten, Comparison of organic (UK'37, TEXH86, LDI) and faunal proxies (foraminiferal assemblages) for reconstruction of late Quaternary sea surface temperature variability from offshore southeastern Australia. *Paleoceanography*. **28**, 377–387 (2013).

43. P. J. Müller, R. Schneider, An automated leaching method for the determination of opal in sediments and particulate matter. *Deep Sea Research I*. **40**, 425–444 (1993).

44. X. Crosta, S. K. Shukla, O. Ther, M. Ikehara, M. Yamane, Y. Yokoyama, Last Abundant Appearance Datum of Hemidiscus karstenii driven by climate change. *Marine Micropaleontology*. **157**, 101861 (2020).

45. X. Crosta, N. Koc, in *Developments in Marine Geology* (2007), vol. Volume 1, pp. 327–369.

46. J. Watt, G. J. Pierce, P. R. Boyle, "Guide to the Identification of North Sea Fish using Premaxillae and Vertebrae" (ICES Cooperative Research Report 220, 1997), p. 231.

47. S. Tercerie, P. Bearez, P. Pruvost, R. Vignes-Lebbe, Osteobase (2019), (available at www.osteobase.mnhn.fr).

48. M. Ghanbarifardi, C. Gut, Z. Gholami, H. R. Esmaeili, C. Gierl, B. Reichenbacher, Osteology of the posterior vertebral column and caudal skeleton of marine amphibious gobies (mudskippers) (Teleostei: Gobioidei). *J Appl Ichthyol*. **36**, 713–723 (2020).

49. A. Filardo, thesis, Hawai'i Pacific University (2019).

50. T. J. Hastie, R. J. Tibshirani, *Generalized additive models* (CRC press, 1990), vol. 43.

51. S. N. Wood, Fast stable restricted maximum likelihood and marginal likelihood estimation of semiparametric generalized linear models. *Journal of the Royal Statistical Society*. **73**, 3–36 (2011).

Acknowledgments: We are grateful to N. Glock and A. Rosskopf for helping with the identification and picking of *Bolivina seminuda* and with R. Macieira, M. Mincarone and P. Béarez for helping in the identification of fish vertebrae. **Funding:** Collaborative Research Project 754 "Climate-Biogeochemistry interactions in the Tropical Ocean" (www.sfb754.de), which is supported by the Deutsche Forschungsgemeinschaft (DFG), Project Humboldt Tipping Point (https://humboldt-tipping.org/en) sponsored by the Federal Ministry of

Education and Research of Germany. FS wishes to thank the DFG for funding through Emmy Noether Nachwuchsforschergruppe ICONOX. **Author contributions:** Conceptualization: RS, RRS, DF. Methodology: RS, PM, TBl, TBa, FS, XC, AB. Writing – original draft: RS, EG, DF, AB. Writing – review & editing: RS, RRS, EG, DF, TBl, TBa, XC, PM, VE, FS, AB. **Competing interests:** Authors declare that they have no competing interests. **Data and materials availability:** All the data will be uploaded to PANGEA.

List of Supplementary Materials

Supplementary Materials

Materials and Methods

Figs. S1 to S10

Tables S1 to S3

References (24–51)

Supplementary Materials for

Smaller fish species in a warm and oxygen-poor Humboldt Current System

Renato Salvatteci, Ralph R. Schneider, Eric Galbraith, David Field, Thomas Blanz, Thorsten Bauersachs, Xavier Crosta, Philippe Martinez, Vincent Echevin, Florian Scholz, Arnaud Bertrand

Correspondence to: rsalvatteci@kms.uni-kiel.de

This PDF file includes:

Materials and Methods

Regional Ocean modelling

The ROMS-PISCES regional model is used to dynamically downscale the coarse-resolution Earth System models (ESM) under the RCP8.5 climate scenario. The model's spatial resolution (~12 km) and numerical schemes allow to represent the Peru upwelling system typical mesoscale features (eddies, filaments, coastline and topographical dynamical effects). ROMS is the Regional Ocean Modelling System (*24*, *25*). It resolves the primitive equations and provides daily three-dimensional temperature, salinity, sea level and velocity fields over the 2006-2100 time period. The model domain covers the coastal region between 5°N and 22°S along Ecuador and Peru, and extends offshore until 95°W. It has 32 levels in the vertical. ROMS is coupled to the Pelagic Interaction Scheme for Carbon and Ecosystem Studies (PISCES) biogeochemical model (*26*). PISCES simulates plankton dynamics with two size classes of phytoplankton and two size classes of zooplankton, as well as the cycle of carbon, of several nutrients (N,P,Si,Fe) and of dissolved oxygen. ROMS-PISCES is forced by boundary conditions and surface atmospheric variables from three Earth System Models (GFDL-ESM2M, IPSL-CM5-LR, CNRM-CM5). To correct ESM systematic bias, boundary conditions are composed of the sum of observed climatological boundary conditions (from the World Ocean Atlas 2009) and of the ESM anomalies, computed as the difference between RCP8.5 conditions and historical conditions (2000-2010 average). For the same purpose, the atmospheric forcing is composed of the sum of the SCOW climatological satellite surface wind (25 km resolution (*26*)) and ESM anomalies with respect to the 2000-2010 average. R-GFDL, R-IPSL, R-CNRM stand for the downscaled solution using ROMS-PISCES of GFDL, IPSL and CNRM, respectively. For more details on the methodology, the reader is referred to (*9*). The SST, oxygen, depth of the 20°C isotherm (a proxy for thermocline depth) and primary production anomalies are computed as differences between two 15-year periods (2086-2100 average minus 2006-2020) in order to filter the ENSO variability that may aliase the fields.

Age model for core M77/2-24

The oceanographic conditions and fish community during the last interglacial off Peru were reconstructed using sediment core M77/2-024-5 (11º05.01´S, 78º00.91´W, water depth 210 m) retrieved off central Peru during Meteor expedition M77/2-2 in 2008 and then stored in GEOMAR core repository. The total length of the core is 1481 cm (Fig. S8). The age model of core M77/2-24 was modified from (*27*) to improve the chronology. The age model for the Holocene period was based on ^{14}C dates while the pre-Holocene age model was done by correlating the grain size and organic carbon records of M77/2-24 with the global benthic $\delta^{18}O$ record (Fig. S9). To better constrain the age model for the last interglacial in core M77/2-24, 49 samples from 1093 to 1388 cm depth were selected and at least 10 specimens of the benthic foraminifera *Bolivina seminuda,* that did not show signs of degradation or alteration, were carefully picked for the $\delta^{18}O$ record. A complete $\delta^{18}O$ record for the entire core could not be obtained due to the absence or poor preservation of benthic foraminifera in other parts of the core. This observation is consistent with similar attempts to date the last interglacial in a core located at 12ºS (*15*). Oxygen isotope measurements were performed at the Leibniz Labor, Christian-Albrechts-University, Kiel. The stacked benthic $\delta^{18}O$ from (*28*) was then compared with the $\delta^{18}O$ record of core M77/2-24 to establish the chronology (Fig. S9). Four tie-points were paired between the stacked $\delta^{18}O$ and the benthic $\delta^{18}O$ record of core M77/2-24 (Fig. S9). Finally, a linear regression between the core depth and the estimated age ($y = 0.107x-7.4277$, $r^2=0.99$) was done to date core M77/2-24. Differences with the previously published chronology are in the order of ~2 to 3 kyr. Paleoceanographic reconstructions off Peru are challenging due to multiple discontinuities and slumping that complicate the development of a robust chronology and the estimation of fluxes (*29*). For this reason, we use concentrations instead of fluxes, but both calculations are shown in Figs. S2 to S4 to support our findings.

Inferred sedimentation rates (SR) in core M77/2-24 range from 9.3 cm × kyr^{-1} during MIS5 to 71.4 cm × kyr^{-1} during the Late Holocene (*30*). Sedimentation rates in M77/2-24 are twice as high as compared with core ODP 680B (*31*) located close to the M77/2-24 site, allowing paleo reconstructions in higher resolution from core M77/2-24. During MIS5 and especially during the last interglacial, sedimentations rates are the lowest during the last 250 kyr (*31*). Lower sedimentation rates during the last interglacial could be due to sediment discontinuities as observed during the Holocene in other sediment cores along the Peruvian coast. The similarity of the $\delta^{18}O$ records in core M77/2-24 and the global benthic stacked record, along with the gradual changes in $\delta^{15}N$, precludes a major impact of sediment discontinuities driving low SR. However, based on the multiple lines of evidence indicating widespread discontinuities in sediments from the Peruvian margin, a cautionary approach is suggested when inferring paleoceanographic conditions based on fluxes of sedimentary components.

Proxy records

Water column denitrification was inferred through $\delta^{15}N$ measurements of sedimentary organic matter. The measurements were done in homogenized and freeze-dried bulk sediment, using a Carlo-Erba CN analyzer 2500 interfaced directly to a Micromass-Isoprime mass spectrometer at the University of Bordeaux. The precision of the isotopic analyses was ±0.25‰. Core M77/2-24 was subsampled every 5 cm, from 1093 to 1478 cm, for $\delta^{15}N$ analysis. Data from the rest of the core was taken from (*27*). Data for the Holocene period from (*32, 33*) is also shown in Fig. S2.

Core M77/2-24 was subsampled every 5 cm for alkenone measurements (total of 294 samples). Alkenones were measured at the Institute of Geosciences in Kiel, Germany. Samples were freeze-dried, homogenized, and extracted using accelerated solvent extraction (Dionex ASE-2000) from 1 g of sediment. The extraction was done using a mixture of dichloromethane (DCM) and methanol (MeOH; 9:1, v:v) as solvents at a pressure of 100 mbar and a temperature of 100 °C. The extracts were purified and analyzed by a double column multidimensional gas chromatograph (Agilent 6890 N) system with two flame ionization detectors using hydrogen as a carrier gas (*34*). Alkenone concentrations were calculated by normalization to two internal standards (*35*). The $U^{K'}_{37}$ was calculated as $C_{37:2}$ / ($C_{37:2}$ + $C_{37:3}$), where $C_{37:2}$ ($C_{37:3}$) represents the amount of the di-unsaturated (tri-unsaturated) alkenones, respectively. Finally, temperatures were reconstructed using the core top calibration of (*36*). The error in temperature estimates based on alkenon*es is ~1 °C* (*37*), while the analytical error in our record is on average less than ±0.1 °C.

Seventy-one extracts were also analyzed to reconstruct ocean water temperatures using the TEX^{H}_{86}. For this, aliquots of the extracts were separated into apolar and polar fractions using aluminum oxide (Al_2O_3) as stationary phase and hexane:DCM (9:1, v:v) and DCM:MeOH (1:1, v:v) as respective eluents. The polar fractions, containing glycerol dialkyl glycerol tetraether (GDGTs), were dried under a gentle stream of nitrogen, re-dissolved in *n*-hexane:2-propanol (99:1, v:v) and filtered through a PTFE filter prior to analysis. GDGTs were analyzed using a Waters HPLC 2695 system coupled to a Micromass ZQ single quadrupole mass spectrometer following the analytical protocol of (*38*) and using the gradient program specified in (*39*). The TEX^{H}_{86} is specifically designed for marine settings with average water temperatures >15 °C, and the core top calibration of (*40*) were used to calculate ocean water temperatures. The TEX_{86} and its derivatives (e.g. TEX^{H}_{86}), which are based on GDGTs produced by Marine Group 1 Crenarchaeota, were originally considered to reflect the temperature of the sea surface water

(*41*). More recent evidence, however, suggests that the TEX_{86} is more likely associated with the temperature at the depth of the chemo-/thermocline (*42*). The temperature difference between the $U^{K'}_{37}$ and the TEX_{86} may hence be attributed to changes in water column stratification, with higher offsets interpreted to indicate a deeper thermocline.

Biogenic silica content was reconstructed by calibrating the silica to titanium (Si/Ti) ratios from the XRF measurements and the biogenic silica percentages obtained by applying an automated leaching method. XRF measurements were done every 1 cm using an Avaatech XRF core scanner, with a generator setting of 10kV. The XRF data of Ti was taken from (*27*), the Si data was not previously published. The automated leaching method was done using sodium hydroxide at a precision of 1–2% (*43*). For this procedure, 37 samples were selected along the core in intervals presenting high, medium, and low contents of biogenic silica. A good correlation between the biogenic silica percentage and the log (Si/Ti) ratios was obtained ($y=0.0106x+0.712$, $r^2=0.52$). This transfer function was applied to the last interglacial section to estimate silica concentrations (Fig. S2c). Biogenic silica from core M77/2-003 was taken from (*16*) .

Sediment processing and diatom slide preparation followed the method described in (*44*). Briefly, the organic matter was digested with H_2O_2 while carbonates were dissolved with HCl, both steps at 65°C until bubbling stops. For each step, the solution was rinsed three times with distilled water under centrifugation during 7 min at 1200 rpm. The aliquot was transferred into a beaker and homogenized into 100 ml of distilled water. Two drops of 150 µl were transferred into a petri dish containing a coverslip and half-filled of distilled water. The petri dish was subsequently filled with distilled water. After 30 min, a wool thread was added to suck the water out of the petri dish overnight. The coverslip was then glued to a slide using optical adhesive

NOA61 that hardens under UV light. Three coverslips were made per sample. Diatom assemblages were determined in 60 samples along core M77/2-24 from 1093 to 1388 cm depth corresponding to 110.7 to 137.8 kyr BP. Samples were taken every 5 cm. At least 300 near complete valves were counted in each sample (> 100 valves per slide from the same sample) on a Nikon 80i phase contrast microscope at a magnification of 1000 X. Counting rules followed the ones described in (*45*). Diatoms were generally identified to the species or species group level. The relative abundance of each species was determined as the fraction of diatom species against total diatom abundance in the sample. Diatoms were classified into six groups of different ecology or living in different systems following (*16*) and references cited therein. First, benthic diatoms living attached to a substratum at the coast. Second, planktonic diatoms thriving in brackish water. Third, planktonic diatoms blooming quickly during the early phase of the upwelling when nutrients are very abundant. Fourth, planktonic diatoms developing during the late phase of the upwelling when nutrient stocks are fading. Fifth, planktonic diatoms living in coastal, nutrient-rich waters out of upwelling systems. And sixth, planktonic diatoms living in oligotrophic waters were nutrient stocks are low. A list of the species or species groups included in each group is given in Table S3.

Sampling for fish debris was done in the same intervals as in the case of the diatom assemblage data. Samples consisted of an average of 41 g of wet material, which yields 16.3 g of dry sediment. Following the sediment subsampling, the samples were heated with a solution of hydrogen peroxide and sodium pyrophosphate for 10 min to disaggregate the organic matter and thereafter were gently washed through a 355 μm sieve (*20*). The remains retained were then stored in an ethanol solution.

The fish debris were quantified and identified with the help of scale and vertebrae collections obtained from recently caught fishes (*11*). Based on pelagic trawls in several transects off Peru, the mesopelagic community of Peru is dominated by the fish families Phosichthyidae (*V.*

lucetia), Myctophidae (especially *Diogenichthys laternatus* and *Lampanyctus idostigma*) and Bathylagidae (especially *Leuroglossus urotranus*) accounting for 60.4, 12.8 and 3.7% of the total abundance, respectively (*19*). The abundance of these species is remarkably high off Peru. For example, the biomass of *V. lucetia* has varied from 2 to 11 million metric tons, an amount similar to that of anchovy. Given the high abundance of mesopelagic fishes it is apparent that a high amount of fish debris from mesopelagic fish must be deposited and preserved in the sediments. Unfortunately, the identification of fish vertebrae from mesopelagic fishes is not an easy task given that lack of vertebrae collections. Some fish vertebrae obtained from fresh fishes and recovered from the sediment samples are shown in Fig. S10. The abundance vertebrae types 1, 2 and 3 is highly correlated (Table S1), suggesting that they belong to the same species. These three types were grouped as goby-like vertebrae (an unidentified species from the Gobiiformes order) based on their small size, the long, narrow-waisted, featureless centra and the lack of prezygapophyses (*46–48*). In addition, the well-defined vertebrae waist, the presence of neural spines and the ossification of these vertebrae suggest that they belong to adults rather than juveniles. The vertebrae of the myctophid *Triphoturus oculeus*, show the distinctive ridges along the vertebrae that characterize the myctophid vertebrae. However, vertebrae from other species from the family of Bathylagidae (i.e. Smooth tongue, *Leuroglossus stilbius*) also show similar ridges along the vertebrae (*49*), making difficult the identification of mesopelagic fish vertebrae. Vertebrae types 4 and 6 lack a defined waist, are less ossified compared to the other vertebrae and thus, they might correspond to juveniles. Type 6 vertebrae are more elongated than type 4 and resemble some characteristics as anchovy vertebrae. Type 5 belong to *V. lucetia*. Type 7 correspond to a hake vertebra. Type 8 correspond to blue lanternfish (*Tarletonbeania crenularis*) according to the findings of (*49*). Type 9 are small and very elongated and perhaps correspond to an eel-shaped fish (e.g. *Nemichthys fronto)*.

The widths of the complete vertebrae per sample were measured and the average per sample is presented in Fig. S3. In order to quantify the effect of degradation, we estimated the "biodegradation over fish vertebrae" index, which estimate the surface of the vertebrae that is not affected by bio-erosion (*20*). This index was calculated per each vertebra, and ranges from 1 to 4. Vertebrae with traces of bio-erosion (e.g. channels) covering between two-thirds and the entire surface were rated as 1, those vertebrae with traces of bio-erosion covering between one-third and two-thirds were rated as 2, those vertebrae with traces of bio-erosion covering up to one-third of the surface were rated as 3, and finally those vertebrae with no sign of bio-erosion were rated as 4. An average per sample interval was done to calculate the biodegradation index where higher values indicate better preservation of the fish vertebrae remains.

Statistical analyses

Differences in fish vertebrae sizes between the last interglacial and Holocene was tested using a non-parametric Mann-Whitney U-test. We used a Generalized Additive Models (GAM (*50*)) to describe the relationship between vertebrae width, and temperature (alkenone-derived SST) and water column denitrification ($\delta^{15}N$, as a proxy for water column deoxygenation). GAM was fitted using the mgcv package (*51*) from the statistic software R (R Development Core Team). The selected model, that considered the interaction between SST and $\delta^{15}N$ (te(SST, $\delta^{15}N$)), was highly significant (p-value<0.000).

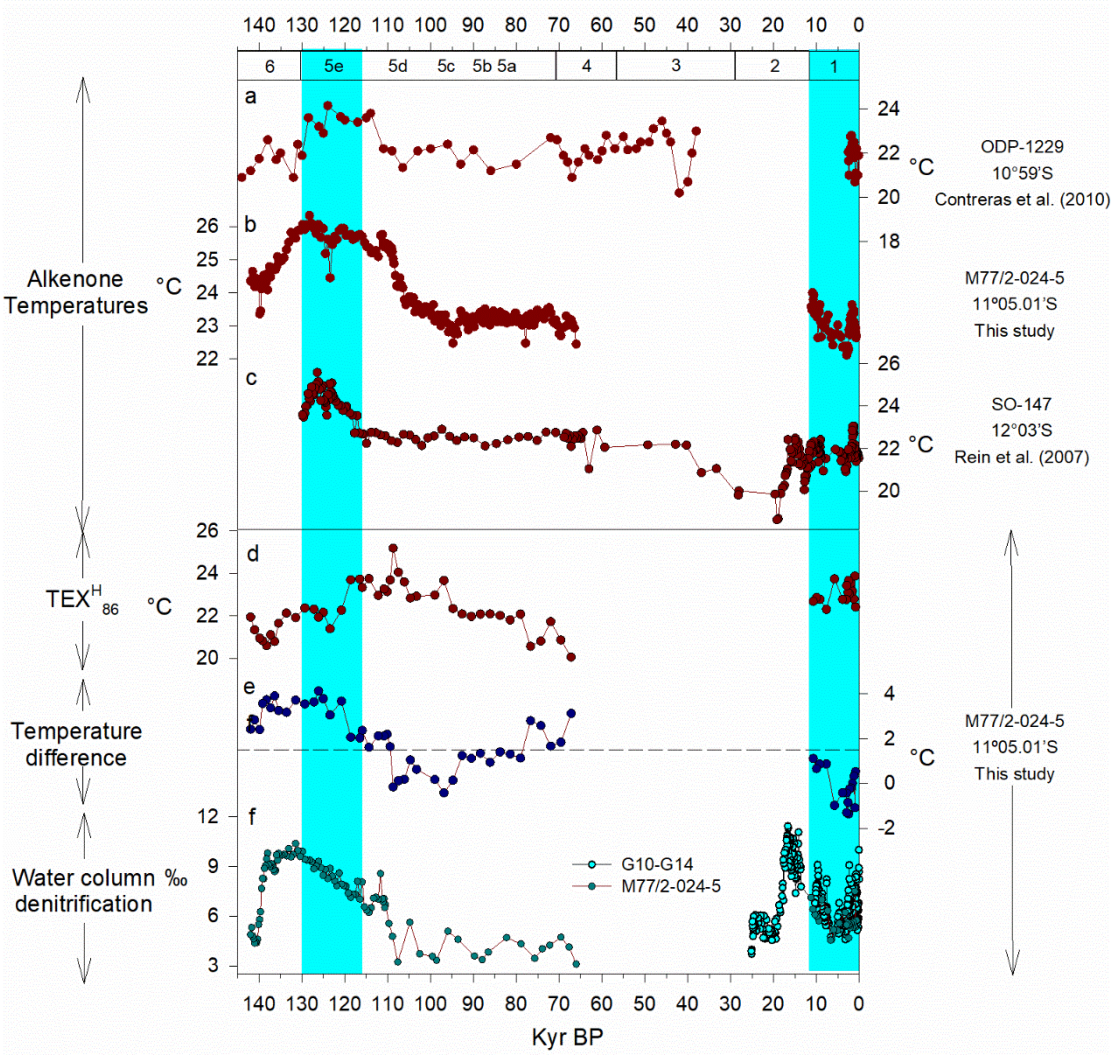

Fig. S1.

Paleoceanographic reconstructions in the Eastern Tropical South Pacific during the last ~145 kyr. a, Alkenone-derived temperature reconstruction, ODP Site 1229 (*14*). **b,** Alkenone-derived temperature reconstruction, M77/2-24 (this study and (*30*) for the Holocene period). **c,** Alkenone-derived temperature reconstruction, SO-147 (*15*). **d,** TEX^{H}_{86}-derived water temperatures M77/2-24 (this study). **e,** Temperature difference between $U^{K'}_{37}$ and TEX^{H}_{86} water temperatures M77/2-24 (this study). **f,** $\delta^{15}N$ as proxy for water column denitrification/nutrient utilization, core M77/2-24 (this study and (*27*)) and the composite record B14-G10-G14 (~14 ºS (*32*)) for the last 25 kyr.

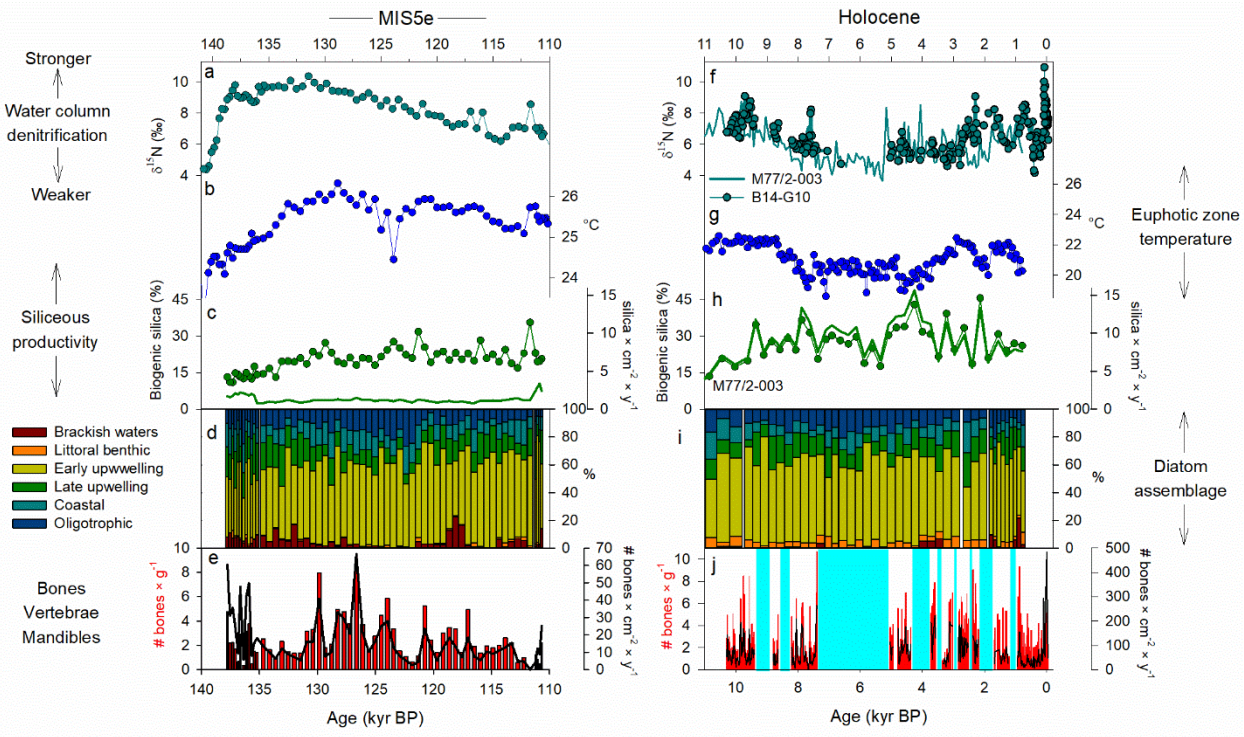

Fig. S2.

Comparison of the last interglacial (a to e, core M77/2-24) and Holocene (f to j, multiple cores) records of ocean and ecosystem changes in the Humboldt Current System. a, and **f,** $\delta^{15}N$ measurements on sedimentary organic matter as a proxy for water column N-loss processes, M77/2-24 for the last interglacial (this study), and cores B14-G10 (*32*) and M77/2-003 (*33*) for the Holocene. **b,** and **g,** Alkenone derived near surface temperature core M77/2-24 for the last interglacial (this study) and M77/2-003 for the Holocene. **c,** and **h,** concentrations (symbols) and fluxes (continuous line) of biogenic silica in M77/2-24 and M77/2-003. **d,** and **i,** diatom assemblages in M77/2-24 (this study) and M77/2-003. **e,** and **j,** Fish bone concentrations (bars) and fluxes (lines). Data in **j** to **t** from core B14-G10 (*11*) retrieved at 14ºS.

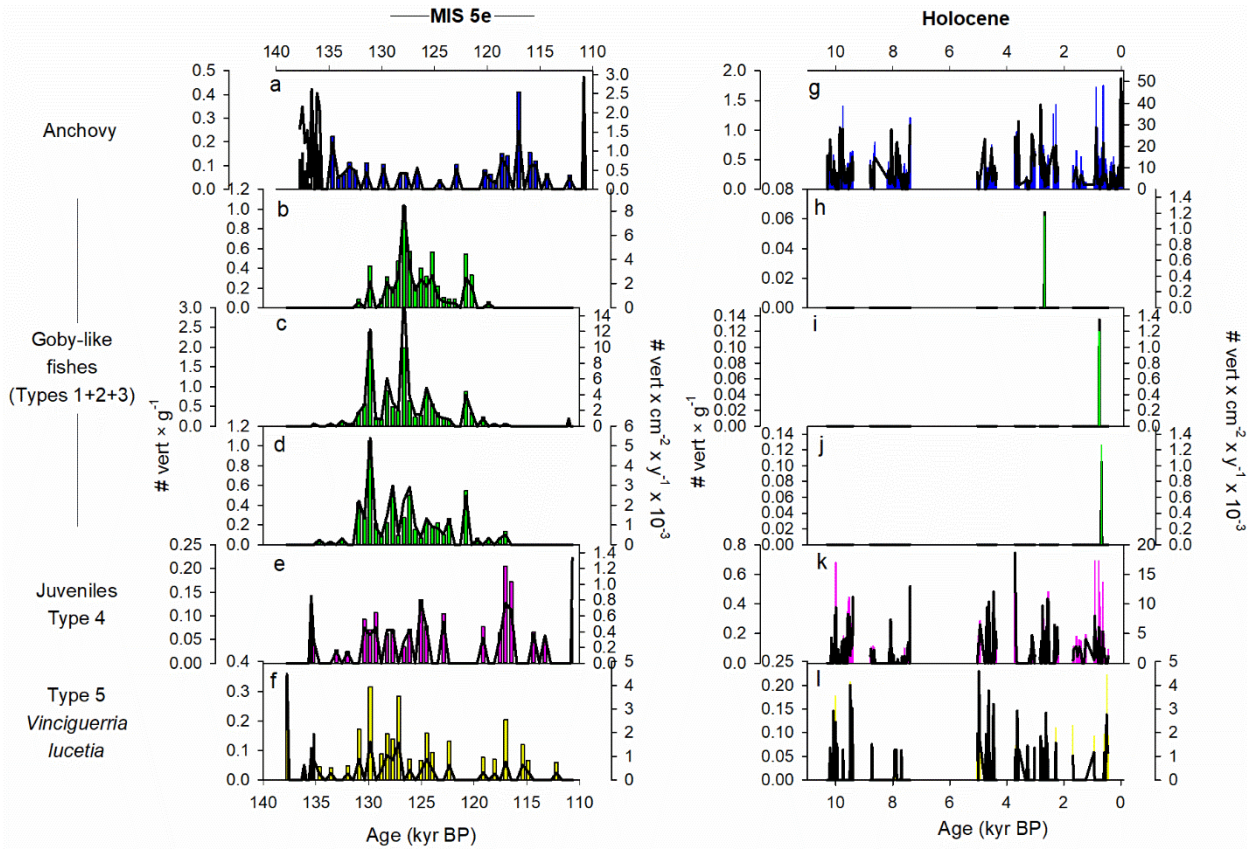

Fig. S3. Comparison of last interglacial (left panels, core M77/2-24) and Holocene (right panels, cores G10-B14) fish bones and fish vertebrae composition in the Humboldt Current System. a, and **g**, Anchovy vertebrae. **b**, and **h**, Type 1 vertebrae. **c**, and **i**, Type 2 vertebrae. **d**, and **j**, Type 3 vertebrae. Types 1, 2 and 3 correspond to goby-like fishes. **e**, and **k**, Type 4 vertebrae, likely belonging to juveniles. **f,** and **l,** *Vinciguerria lucetia* concentrations (bars) and fluxes (lines). Fish debris are expressed as concentrations (bars) and fluxes (solid lines).

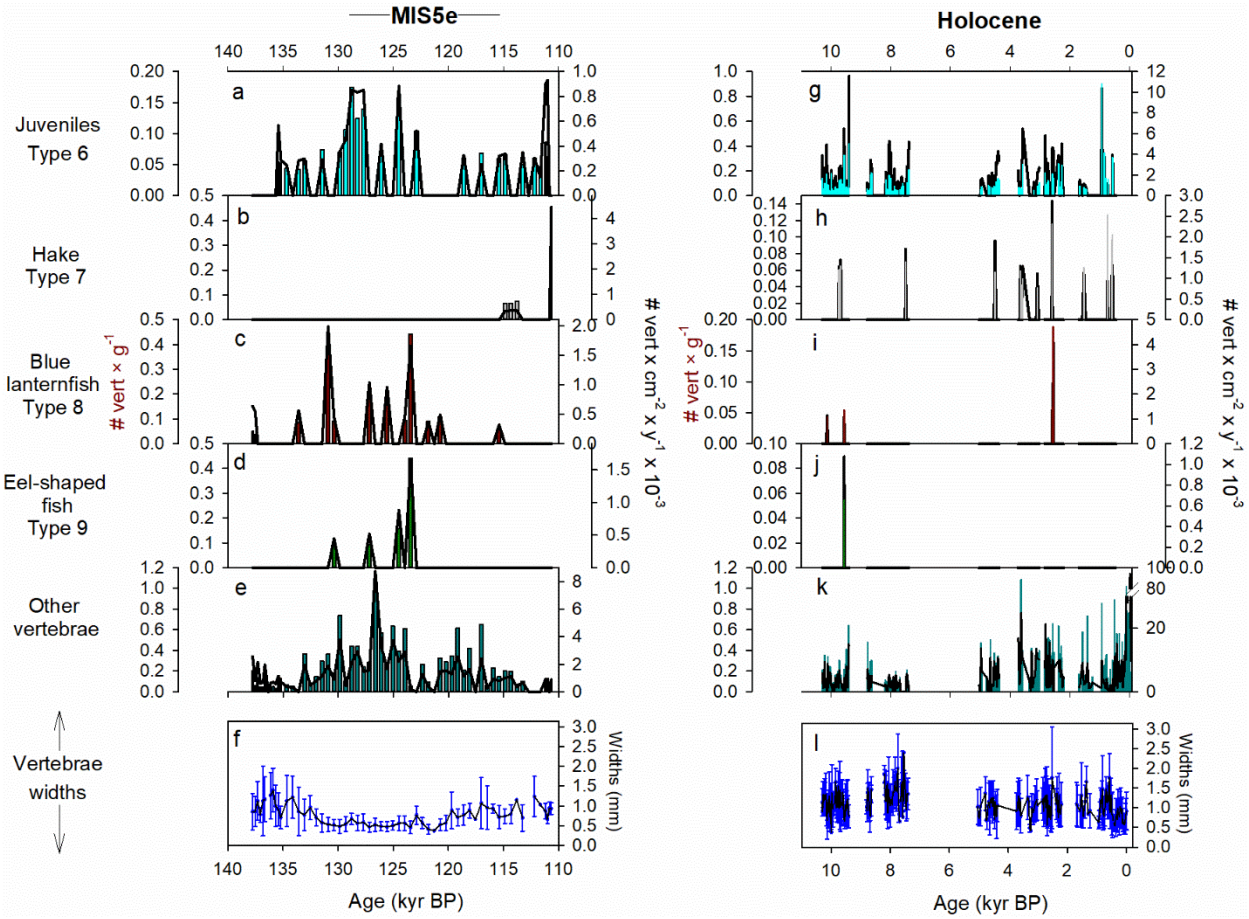

Fig. S4. Comparison of last interglacial (left panels, core M77/2-24) and Holocene (right panels, cores G10-B14) fish bones and fish vertebrae composition in the Humboldt Current System and vertebrae widths. a, and **g**, Type 6, likely belonging to juveniles. **b**, and **h**, Type 7 vertebrae corresponding to hake (*Merluccius gayi peruanus*). **c**, and **i**, Type 8 vertebrae belonging to the mesopelagic fish blue lanternfish. **d**, and **j**, Type 9 vertebrae of an eel-shaped fish. **e**, and **k**, Other vertebrae. **f, and l,** Average of the vertebrae widths of all species. Fish debris are expressed as concentrations (bars) and fluxes (solid lines). Note the different scales.

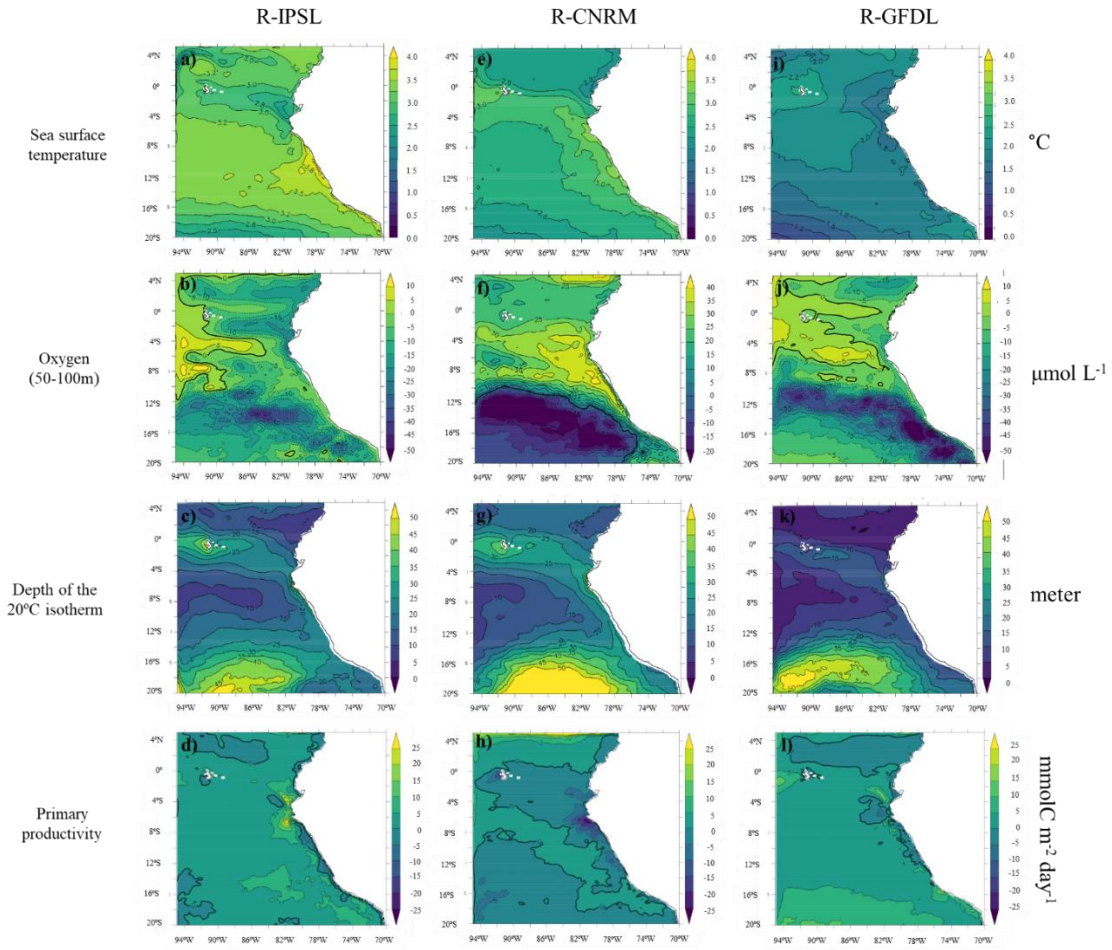

Fig. S5.

Model projections (2086-2100 average minus 2006-2020 average) of sea surface temperature, oxygen concentration, depth of the 20°C and primary productivity (0-500 meters) for the RCP 8.5 scenario in three Earth system models. a-d, Regional simulations using the IPSL Earth System model. **e-h,** Regional simulations using the CNRM Earth System model. **i-l,** Regional simulations using the GFDL Earth System model. The colour scale is similar for a given projection among the different Earth System models, except in **f**.

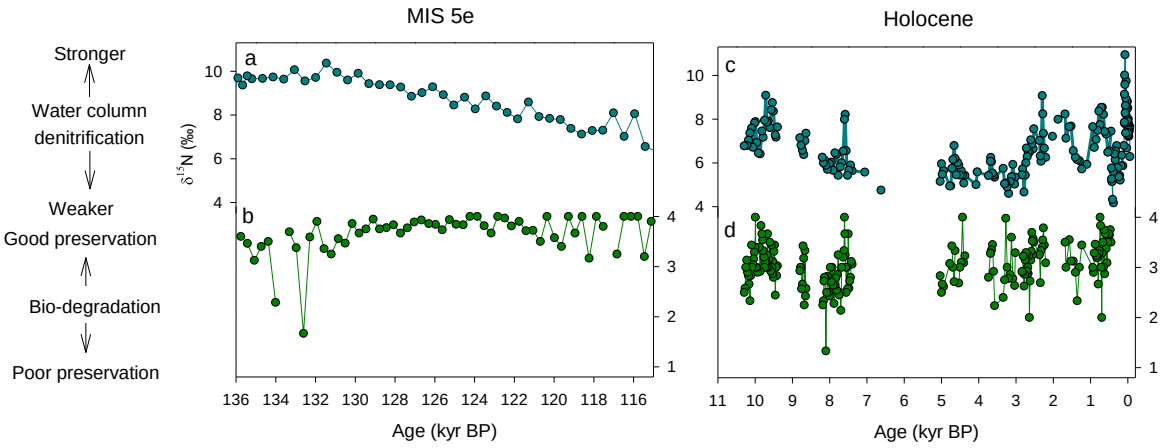

Fig. S6.

Comparison of water column denitrification and fish vertebrae preservation during last interglacial (M77/2-24) and the Holocene (B14-G10). **a,** Record of water column denitrification (this study). **b,** Bio-degradation index on all fish vertebrae for the last interglacial (this study). **c,** Record of water column denitrification in the composite record B14-G10. **d,** Bio-degradation index on all fish vertebrae in core G10 (*11*). During the last interglacial the inferred average preservation (3.7±0.4, n=928) was higher than during the Holocene (3±0.4, n= 2689). In sediment samples covering the las 25 kyr BP there is a strong correlation between the bio-erosion index and $\delta^{15}N$ that suggests that a more oxygenated water column may allow bio-eroders to colonize scales in the water column or shortly after arrival to the sediments (*11*). Higher $\delta^{15}N$ values and thus stronger water column denitrification during the last interglacial might have promoted a good preservation of fish vertebrae.

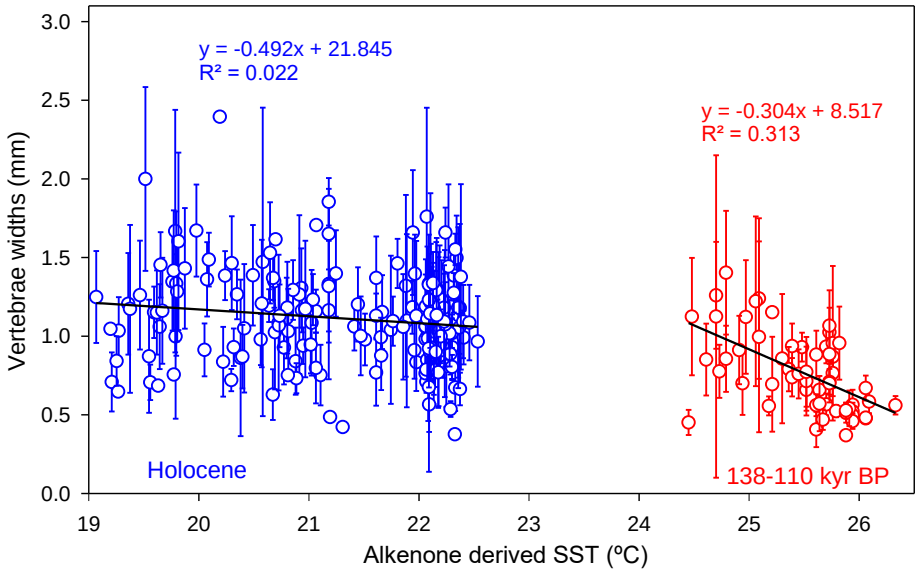

Fig. S7.

Small fishes in a warm ocean. Average (±2 standard error) of fish vertebrae widths per sample vs alkenone derived SST for the Holocene (M77/2-003 taken at 15ºS (*30*)) and the period between 138 to 110 kyr BP (this study). During the Holocene, the SST ranged between 19.5-22.5 ºC and no trend was found between vertebrae size and temperature, whereas only exceedingly small vertebrae were found at temperatures around ~26 ºC during the last interglacial.

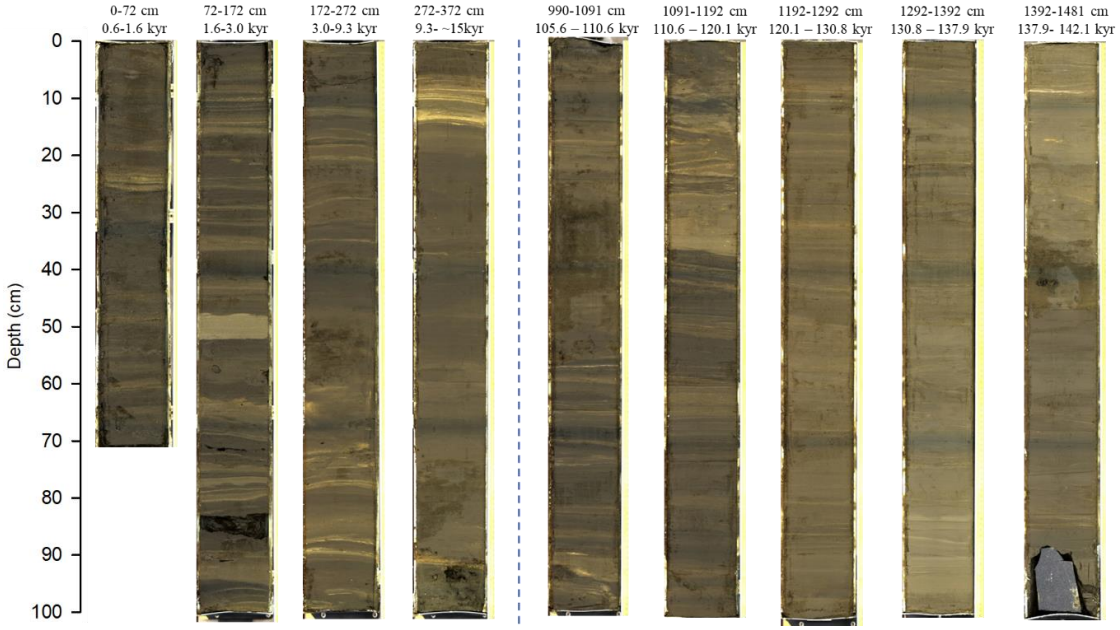

Fig. S8.

Photographic images of the sections corresponding to the Holocene and MIS5 of core M77/2-24. The first 3 meters of core M77/2-24 are characterized by dark olive gray clay interbedded with olive to yellow silty clay laminations. From 3 to 10 meters depth the sediments are darker and characterized by sections with massive to bioturbated sediments, some olive to pale yellow silty clay laminations are visible in this interval (sections not shown). From ~10 to 14.5 m the sediments are paler compared to the first 3 meters, contain laminations, specially from 11.6 to 13.5 meters depth.

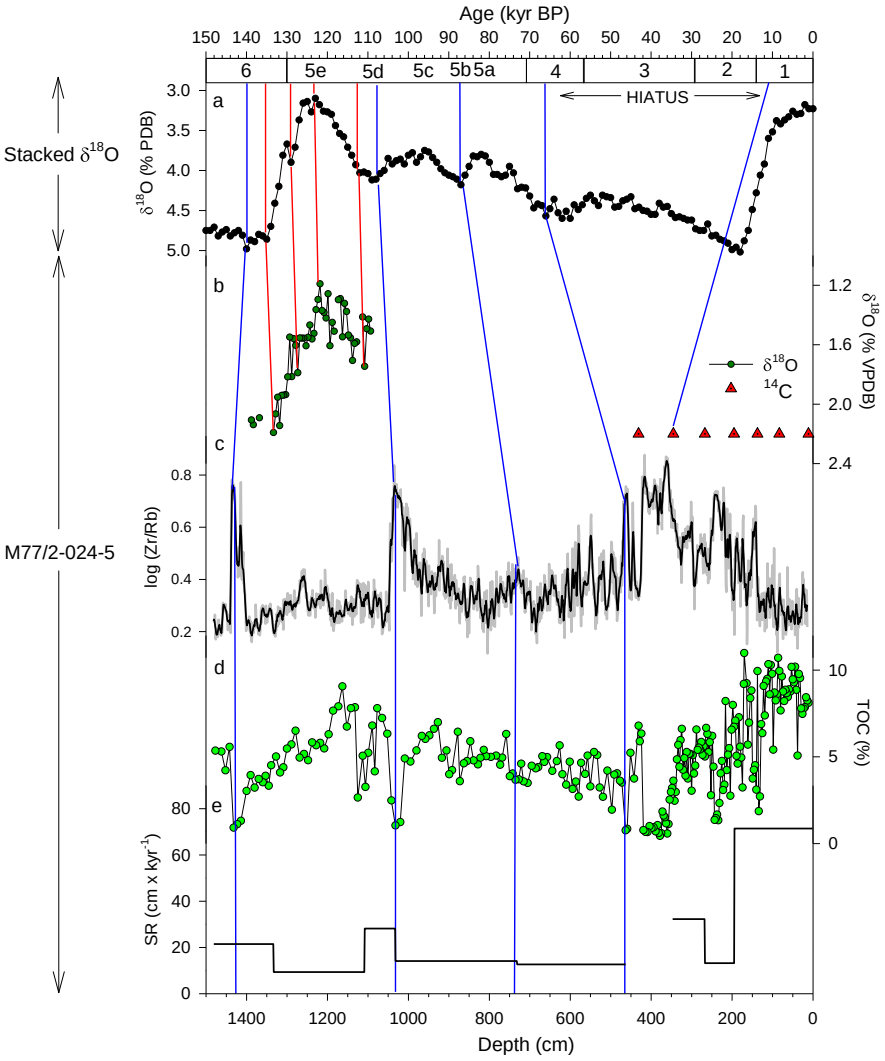

Fig. S9.

Age model of core M77/2-24 based on $\delta^{18}O$, ^{14}C and correlation of grain sizes with the global benthic $\delta^{18}O$ record. a, Global stacked benthic $\delta^{18}O$ record (*28*). **b,** $\delta^{18}O$ values of the benthic foraminifera *Bolivina seminuda*; red triangles indicate ^{14}C ages. **c,** Sedimentary log Zr/Rb ratio. **d,** Total organic carbon (TOC) percentages. **e,** Sedimentation rates (SR, cm × kyr^{-1}). Blue lines indicate correlations based on the log Zr/Rb ratio and the stacked $\delta^{18}O$ record, while red lines indicate the tie points between the stacked $\delta^{18}O$ and the benthic $\delta^{18}O$ record of core M77/2-24. Data in **c** and **d** taken from (*27*).

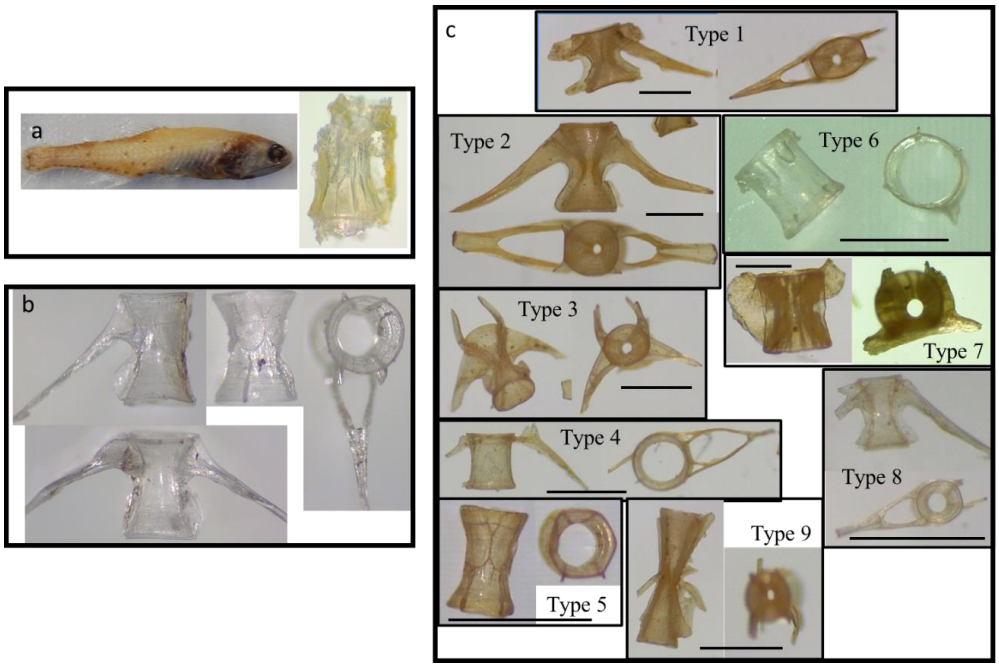

Fig. S10.

Comparison of vertebrae obtained from fresh fish and vertebrae found in the sediment record. a, Photograph of the myctophid *Triphoturus oculeus*, (4 cm total length) and a vertebra (0.5 mm, vertebrae width) taken from the same fish. **b**, Multiple vertebrae from *Vinciguerria lucetia* retrieved from a living specimen collected off Callao (12ºS). **c**, Most abundant vertebrae found in cores G-10 and M77/2-24 (modified from (*11*)). The scale bar in c, represents 1 mm.

	Anchovy/g	Type 1/g	Type 2/g	Type 3/g	Type 4/g	Type 5/g	Type 6/g	Type 7/g	Type 8/g	Type 9/g	non-identified/g	scale fragments/g	fish bones/g	spines/g	spine fragments/g	mandibles/g
Anchovy/g	1.00															
Type 1/g (goby-like fish)	-0.13	1.00														
Type 2/g (goby-like fish)	-0.12	0.78	1.00													
Type 3/g (goby-like fish)	-0.19	0.75	0.78	1.00												
Type 4/g (juveniles)	-0.12	0.19	0.35	0.26	1.00											
Type 5/g (*Vinciguerria lucetia*)	0.02	0.35	0.42	0.31	0.23	1.00										
Type 6/g (juveniles)	0.06	0.17	0.23	0.23	0.31	0.36	1.00									
Type 7/g (hake)	-0.16	-0.18	-0.23	-0.20	0.10	-0.11	-0.07	1.00								
Type 8/g (Blue lanternfish)	-0.18	0.32	0.28	0.34	-0.26	0.13	-0.27	-0.13	1.00							
Type 9/g (eel-shaped fish)	-0.17	0.27	0.36	0.36	0.10	0.12	-0.02	-0.07	0.41	1.00						
non-identified/g	0.04	0.59	0.64	0.42	0.28	0.48	0.17	-0.03	0.11	0.08	1.00					
scale fragments/g	0.31	0.00	-0.02	-0.10	0.17	0.21	0.12	-0.06	0.01	-0.01	0.19	1.00				
fish bones/g	0.44	0.20	0.20	0.17	0.18	0.27	-0.06	0.11	0.11	0.13	0.40	0.31	1.00			
spines/g	0.45	-0.01	0.02	-0.01	-0.03	0.25	0.16	0.03	-0.15	0.02	0.16	0.43	0.48	1.00		
spine fragments/g	0.43	-0.37	-0.33	-0.30	-0.06	-0.07	-0.21	0.01	-0.02	-0.08	-0.15	0.21	0.37	0.20	1.00	
mandibles/g	-0.07	0.28	0.37	0.37	0.27	0.13	0.33	-0.04	-0.03	0.21	0.31	0.01	0.19	0.05	-0.11	1.00

Table S1.

Correlation between fish vertebrae concentrations in core M77/2-24. Correlation values (rs) between the different types of fish vertebrae concentrations and fish bones (No. of fish debris × g^{-1}) from 137.8 to 110.7 kyr BP in core M77/2-24. Statistically significant values ($p<0.05$) are underlined.

Vertebrae	MIS5e		Holocene		*U*	p-value
	average (mm)	n	average (mm)	n		
All species	0.58	643	1.09	2488	259218	***<0.0001***
Anchovy	1.37	29	1.43	1306	17513	*0.49*
Goby-like fishes	0.50	352	0.91	3	35	***0.01***
Vinciguerria lucetia	0.60	29	0.61	51	691	*0.63*
Blue lanternfish	0.35	12	0.50	6	16	*0.06*
Other species	0.62	221	0.72	1121	94543	***<0.0001***

Table S2.

Results of the Mann-Whitney U test of the vertebrae widths between the last interglacial (MIS5e) and Holocene periods. Bold and underlined values indicate significance (p=<0.05).

Benthic diatom group	Brackish water diatom group	Early Upwelling diatom group	Late Upwelling diatom group	Planktonic eutrophic	Planktonic oligotrophic
Amphora spp	*Cyclotella* spp	*Chaetoceros vegetative* spp	***Chaetoceros RS form 3***	*Actinocyclus* spp	*Alveus marinus*
***Biddulphia* spp**	***C. striata***	*C. cinctus vegetative celles*	*CRS form 5*	***A. curvatulus***	***Azpeitia africana***
B. alternans	***C. stylorum-litoralis***	*C. didymus vegetative cells*	***CRS affinis***	*A. exigus*	***A. nodulifera***
***Cocconeis* spp**		***Chaetoceros RS form 1***	***CRS diadema***	*A. octonarius*	*A. tabularis*
C. california		***CRS form 2***	***CRS lorenzianus***	*Actinoptychus argus*	***Ditylum brightwellii***
C. costata		***CRS form 4***	*Thalassionema bacillare*	*A. campanulifer*	*Nitzschia* spp
C. dirupta		*CRS coronatus*	*T. nitzschioides* var *capitulata*	***A. minutus***	*N. bicapitata*
C. distans		*CRS debilis*	***T. nitzschioides* var *claviformis***	*A. parvus*	*N. capuluspalae*
C. placentula		*Minidiscus chilensis*	*T. nitzschioides* var *inflata*	***A. senarius***	*N. interrupestriata*
C. scutellum		***Skeletonema* spp**	*T. nitzschioide* var *lanceolata*	*A. vulgaris*	*N. ovalis*
Delphineis karstenii			***T. nitzschioides* var *nitzschioides***	*Asteromphalus* spp	*N. sicula*
Diploneis spp				*A. arachne*	*Planktonellia sol*
Eucampia spp				*A. flabellatus*	*Proboscia alata*
Navicula spp				*Coscinodiscus* spp	*Pseudosolenia calcaravis*
Odontella spp				*C. asteromphalus*	*Rhizosolenia* spp
Paralia sulcata				*C. centralis*	*R. acicularis*
Pinnularia spp				*C. concinnus*	*R. acuminata*
Plagiogrammopsis vanheurckii				*C. decrescens*	*R. bergonii*
Pleurosigma spp				*C. gigas*	*R. castracanei*
Trachyneis spp				***C. radiatus***	*R. clevei*
Triceratium spp				*Fragilariopsis doliolus*	*R. decipiens*
Raphid pennate spp				*Hemiaulus* spp	*R. hyalina*
				Hemidiscus cuneiformis	*R. imbricata*
				Pseudo-Nitzschia pungens	*R. setigera*
				Thalassiosira exigua	***Roperia tessalata***
				T. oceanica	*Stellarima stellaris*
				T. pacifica	*Stephanopyxis* spp
					Thalassionema frauenfeldii
					T. javanicum
					T. nitzschioides var *parva*
					Thalassiosira spp
					***T. eccentrica* gp**
					***T. leptopus* gp**
					***T. oestrupii* gp**
					T. simonsenii
		RS = resting spores			***Thalassiothrix longissima***

Table S3.

List of the species or species groups used to classify the diatom assemblages in core

M772-24

References

24. P. Penven, L. Debreu, P. Marchesiello, J. C. McWilliams, Evaluation and application of the ROMS 1-way embedding procedure to the central California upwelling system. *Ocean Modelling*. **12**, 157–187 (2006).

25. A. F. Shchepetkin, J. C. McWilliams, Correction and commentary for "Ocean forecasting in terrain-following coordinates: Formulation and skill assessment of the regional ocean modeling system" by Haidvogel et al., J. Comp. Phys. 227, pp. 3595–3624. *Journal of Computational Physics*, 16 (2009).

26. C. M. Risien, D. B. Chelton, A Global Climatology of Surface Wind and Wind Stress Fields from Eight Years of QuikSCAT Scatterometer Data. *Journal of Physical Oceanography*. **38**, 2379–2413 (2008).

27. F. Scholz, J. McManus, A. Mix, C. Hensen, R. Schneider, The impact of ocean deoxygenation on the ocean's iron supply. *Nature Geoscience*. **7**, 433–437 (2014).

28. L. E. Lisiecki, M. E. Raymo, A Pliocene-Pleistocene stack of 57 globally distributed benthic δ18O records. *Paleoceanography*. **20**, PA1003 (2005).

29. R. Salvatteci, D. Field, A. Sifeddine, L. Ortlieb, V. Ferreira, T. Baumgartner, S. Caquineau, F. Velazco, J. L. Reyss, J. A. Sanchez-Cabeza, D. Gutierrez, Cross-stratigraphies from a seismically active mud lens off Peru indicate horizontal extensions of laminae, missing sequences, and a need for multiple cores for high resolution records. *Marine Geology*. **357**, 72–89 (2014).

30. R. Salvatteci, R. R. Schneider, T. Blanz, E. Mollier-Vogel, Deglacial to Holocene Ocean Temperatures in the Humboldt Current System as Indicated by Alkenone Paleothermometry. *Geophysical Research Letters*. **46** (2019), doi:10.1029/2018gl080634.

31. G. Wefer, P. Heinze, E. Suess, in *Proceedings of the Ocean Drilling Program, Scientific Results, Vol. 112* (1990).

32. R. Salvatteci, D. Gutierrez, A. Sifeddine, L. Ortlieb, E. Druffel, M. Boussafir, R. Schneider, Centennial to millennial-scale changes in oxygenation and productivity in the Eastern Tropical South Pacific during the last 25 000 years. *Quaternary Science Reviews*. **131**, 102–117 (2016).

33. E. Mollier-Vogel, P. Martinez, T. Blanz, R. Robinson, S. Desprat, J. Etourneau, K. Charlier, R. Schneider, Mid-Holocene deepening of the Southeast Pacific oxycline. *Global and Planetary Change*. **172**, 365–373 (2018).

34. J. Etourneau, R. Schneider, T. Blanz, P. Martinez, Intensification of the Walker and Hadley atmospheric circulations during the Pliocene–Pleistocene climate transition. *Earth and Planetary Science Letters*. **297**, 103–110 (2010).

35. T. Blanz, K.-C. Emeis, H. Siegel, Controls on alkenone unsaturation ratios along the salinity gradient between the open ocean and the Baltic Sea. *Geochimica et Cosmochimica Acta*. **69**, 3589–3600 (2005).

36. P. J. Müller, G. Kirst, G. Ruhland, I. von Storch, A. Rosell-Melé, Calibration of the alkenone paleotemperature index U37K` based on core-tops from the eastern South Atlantic and the global ocean (60ºN-60ºS). *Geochimica et Cosmochimica Acta*. **62**, 1757–1772 (1998).

37. G. Leduc, R. Schneider, J.-H. Kim, G. Lohmann, Holocene and Eemian sea surface temperature trends as revealed by alkenone and Mg/Ca paleothermometry. *Quaternary Science Reviews*. **29**, 989–1004 (2010).

38. E. C. Hopmans, S. Schouten, R. D. Pancost, J. S. S. Damste, Analysis of intact tetraether lipids in archaeal cell material and sediments by high performance liquid chromatography/atmospheric pressure chemical ionization mass spectrometry. *Rapid Commun. Mass Spectrom.*, 5 (2000).

39. X.-L. Liu, R. E. Summons, K.-U. Hinrichs, Extending the known range of glycerol ether lipids in the environment: structural assignments based on tandem mass spectral fragmentation patterns: Extending the known range of glycerol ether lipids in the environment. *Rapid Commun. Mass Spectrom.* **26**, 2295–2302 (2012).

40. J.-H. Kim, New indices and calibrations derived from the distribution of crenarchaeal isoprenoid tetraether lipids: Implications for past sea surface temperature reconstructions. *Geochimica et Cosmochimica Acta*, 16 (2010).

41. S. Schouten, E. C. Hopmans, E. Schefuß, J. S. Sinninghe Damsté, Distributional variations in marine crenarchaeotal membrane lipids: a new tool for reconstructing ancient sea water temperatures? *Earth and Planetary Science Letters*. **204**, 265–274 (2002).

42. R. A. Lopes dos Santos, M. I. Spooner, T. T. Barrows, P. De Deckker, J. S. Sinninghe Damsté, S. Schouten, Comparison of organic (UK'37, TEXH86, LDI) and faunal proxies (foraminiferal assemblages) for reconstruction of late Quaternary sea surface temperature variability from offshore southeastern Australia. *Paleoceanography*. **28**, 377–387 (2013).

43. P. J. Müller, R. Schneider, An automated leaching method for the determination of opal in sediments and particulate matter. *Deep Sea Research I*. **40**, 425–444 (1993).

44. X. Crosta, S. K. Shukla, O. Ther, M. Ikehara, M. Yamane, Y. Yokoyama, Last Abundant Appearance Datum of Hemidiscus karstenii driven by climate change. *Marine Micropaleontology*. **157**, 101861 (2020).

45. X. Crosta, N. Koc, in *Developments in Marine Geology* (2007), vol. Volume 1, pp. 327–369.

46. J. Watt, G. J. Pierce, P. R. Boyle, "Guide to the Identification of North Sea Fish using Premaxillae and Vertebrae" (ICES Cooperative Research Report 220, 1997), p. 231.

47. S. Tercerie, P. Bearez, P. Pruvost, R. Vignes-Lebbe, Osteobase (2019), (available at www.osteobase.mnhn.fr).

48. M. Ghanbarifardi, C. Gut, Z. Gholami, H. R. Esmaeili, C. Gierl, B. Reichenbacher, Osteology of the posterior vertebral column and caudal skeleton of marine amphibious gobies (mudskippers) (Teleostei: Gobioidei). *J Appl Ichthyol*. **36**, 713–723 (2020).

49. A. Filardo, thesis, Hawai'i Pacific University (2019).

50. T. J. Hastie, R. J. Tibshirani, *Generalized additive models* (CRC press, 1990), vol. 43.

51. S. N. Wood, Fast stable restricted maximum likelihood and marginal likelihood estimation of semiparametric generalized linear models. *Journal of the Royal Statistical Society*. **73**, 3–36 (2011).